

Experimental and numerical investigation of three-dimensional shock train topology with differently oriented background waves

Dayi Wang ¹, Ziao Wang ^{1,*}, Juntao Chang,¹ Lianjie Yue,² Gang Wang ³ and Hao Chen ²

¹Harbin Institute of Technology, Harbin 150001, People's Republic of China

²State Key Laboratory of High Temperature Gas Dynamics, Institute of Mechanics, Chinese Academy of Sciences, Beijing 100190, People's Republic of China

³Hypervelocity Aerodynamics Institute, China Aerodynamics Research and Development Center, Mianyang 621000, People's Republic of China



(Received 21 August 2023; accepted 21 December 2023; published 13 February 2024)

To better understand the three-dimensional topology of the interaction between the shock train and the background wave, the steady and dynamic characteristics of a shock train were investigated using wind-tunnel experiments and numerical simulation. A 14° wedge placed at the bottom and sidewalls was used to generate background waves traveling in different directions. Mounting the wedge on the bottom wall at an incoming Mach number of 1.85 leads to the formation of two symmetric and two asymmetric λ -shaped shock train leading shocks (STLSs), while an incoming Mach number of 2.70 results in one symmetric and two asymmetric X-shaped STLSs. The shock train, which runs perpendicular to the background wave, is always symmetrical at an incoming Mach number of 1.85 when the wedge is mounted on the lateral wall. A flow phenomenon in which the STLS transforms from asymmetric to symmetric after undergoing rapid movement is observed at an incoming Mach number of 2.70. The mean and root-mean-square (rms) pressure profiles confirm the morphological transformation of the STLS. The dynamic properties of the shock train are analyzed by combining the STLS trajectory with the transient wall pressure. Power spectral-density analysis reveals that the frequency of pressure oscillations is independent of whether the shock train is in the same flow cross section as the background wave and depends only on the incoming Mach number and the backpressure. The three-dimensional steady-state numerical simulation reveals the mutual interference structure of the background wave and shock train.

DOI: [10.1103/PhysRevE.109.025103](https://doi.org/10.1103/PhysRevE.109.025103)

I. INTRODUCTION

Scramjets are ideal powered devices for air-breathing hypersonic propulsion that have become a popular research topic in the quest for high-speed flight in many countries [1–5]. The inlet, which links the hypersonic vehicle to its propulsion system, is a key component of the scramjet engine, and its aerodynamic characteristics and performance play important roles in the propulsion system. In an air-breathing engine, the incoming air is subjected to a series of compressions that are collectively referred to as the shock train and provide continuous flow conditions within the combustion chamber. The structure of the shock train is complex, with strong three-dimensional characteristics, and its behavior is strongly dependent on a multitude of factors: the incoming Mach number [6], boundary layer momentum thickness [7], and chamber backpressure [8]. Consequently, extensive investigation of the dynamic characteristics of the shock train has been performed using various methods, including theoretical analysis [9–11], wind tunnel experiments [12–14], and numerical simulation [15–17].

The position of the shock train is important in matching the inlet with the combustion chamber and is used to determine the safety margin of an engine [18,19]. Billig *et al.* [20,21]

developed a mathematical model (the Billig formula) from which the position of the shock train leading shock (STLS) could be ascertained, with results revealing that the position of the STLS is jointly determined by the incoming Mach number, boundary-layer momentum thickness, momentum thickness Reynolds number, duct characteristic length, and backpressure ratio. Other researchers such as Matsuo *et al.* [22] and Gnani [23] have also comprehensively reported morphological structures of the shock train, with results suggesting the existence of two types of shock trains, normal and oblique, of which normal symmetric shock trains occur at low Mach numbers and oblique asymmetric shock trains are observed as the Mach number increases. The backpressure resistance differs for each structure.

The shock train exhibits unsteady characteristics that are sensitive to pressure fluctuations and vortex shedding in the separation zone. Bruce *et al.* [24] investigated the evolution of shock trains in a parallel-walled duct over a backpressure disturbance frequency range of 16–90 Hz via both experiment and numerical simulation, with results indicating that the unsteady Reynolds-averaged Navier-Stokes scheme agrees with the experimental data at lower forced frequencies (~ 40 Hz), whereas numerical simulation could not accurately reproduce the separation region that forms in an unsteady shock train. Experimental investigation of the response of a shock train to high-frequency backpressure excitation (between 105 and 225 Hz) by Xiong *et al.* [25,26] showed that the oscillation

*Corresponding author: 1360211958@qq.com

frequency of a shock train is similar to the excitation frequency of the backpressure, meaning that the pressure measurement could be used to determine the motion of the shock train. Fievet *et al.* [27] quantified the effect of the inflow confinement ratio on the structure of a normal shock train using direct numerical simulation (DNS) in a rectangular cross-sectional channel, with results indicating that increasing the inflow confinement ratio leads to gradual upstream movement of the shock train. Furthermore, increasing the boundary-layer momentum thickness was found to result in the formation of weakly bifurcated shock trains of extended length. Wang *et al.* [28] investigated the structure and motion of an oblique shock train in a hypersonic wind tunnel. Analysis of the upstream motion by synchronized schlieren imaging with pressure measurement data showed the transition from a symmetric to an asymmetric structure during throttling. Inherent oscillatory properties were also observed in the oblique shock train.

The shock train in a working scramjet engine is highly three dimensional. Early studies were restricted to traditional shadow techniques that could only provide information on the flow field in the streamwise cross section. However, the development of numerical simulation and advanced experimental techniques has enabled direct observation of the three-dimensional topology of the shock train. Mousavi *et al.* [29] carried out three-dimensional numerical simulations of a shock train in a convergent-divergent nozzle to understand the behavior and position variations of the shock train. The data obtained using the Reynolds-stress model matched the experimental data, indicating that the total incoming temperature and heat generation rate significantly affect the position of the STLS. Kamali *et al.* [30] used the large-eddy simulation (LES) method to study the evolution of a shock train in a convergent-divergent nozzle, with the accuracies of three subgrid models assessed at identifying the STLS. The results demonstrated more accurate predictions for the algebraic wall-modeled LES than the Smagorinsky-Lilly and wall-adapting local-eddy viscosity models. Geerts *et al.* [31,32] investigated the three-dimensional properties of the STLS both experimentally and numerically using different rectangular aspect ratios. Quantification of the global density-gradient variation with the background-oriented schlieren method indicated that the lower momentum thickness of the long-axis boundary layer renders it more likely to separate than the short-axis boundary layer. Hunt *et al.* [33] used stereo particle-image velocimetry (PIV) to investigate the instability properties of a shock train under structural transitions from oblique to normal and revealed the three-dimensional structure of a λ -type shock train. Gnani *et al.* [34,35] explored the effect of three different turbulence models with respect to the evolutionary process of the shock train and found that the k - ω Wilcox model was able to accurately reproduce the flow structure in the vicinity of the wall. As observed from the numerical results obtained for the streamwise cross section, the intensity of the STLS is the same in both two- and three-dimensional cases. However, the thinner boundary layer in the three-dimensional case allows the flow to expand further into the subsonic region, resulting in a stronger deceleration of the flow behind the STLS. Recently, Edelman *et al.* [36] combined information obtained from high-speed schlieren imaging with wall static pressure measurement, surface oil flow visualization, and PIV in the

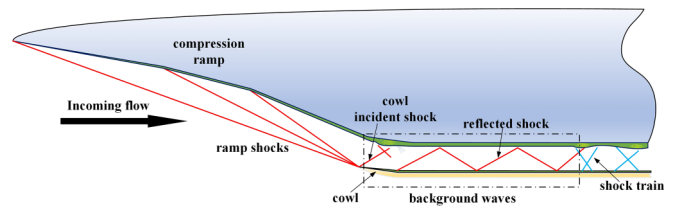


FIG. 1. Illustration of a hypersonic inlet/isolator.

three-dimensional modeling of a shock train. The undisturbed flow in the isolator indicates the existence of a large-scale streamwise vortex at the sidewall that extends downstream from the asymmetric nozzle. The vortex extracts momentum from the layer attached at the sidewall, separating it from the corner front and causing the separation bubble to move upward in response to the inverse pressure gradient, ultimately skewing the region in which the shock wave–boundary layer interacts.

Generally, the inlet and isolator are connected by a geometric throat. As depicted in Fig. 1, the incoming flow is initially compressed by the inlet to generate an incident shock that is continuously reflected between the upper and lower walls of the isolator, resulting in a complex background wave. Tan *et al.* [37] were the first to refer to the shock, compression, and expansion waves formed within the isolator together as background waves. They found that these waves induce large streamwise and transverse pressure gradients upstream of the shock train, with results showing that the coupling effect between the shock train and background wave becomes significant as the upstream Mach number increases. Three instability states were discovered for large-scale oscillations of the shock train. Xu *et al.* [38] used numerical simulation to study the flow process of the backpressure-induced separation of an oblique shock train and observed rapid forward movement when the separation point of the STLS exceeds the reflection point of the background wave. Subsequently, Li *et al.* [39,40] confirmed jump behavior for a shock train by installing a wedge upstream of the isolator to simulate the generation of background waves in a direct-connect tunnel experiment. A low-order dynamic model was constructed that utilized the free-interaction theory with one-dimensional analysis, providing a theoretical analysis of the rapid forward movement of the shock train. Huang *et al.* [41] introduced a background wave into a curved channel to investigate the effect of curvature on a shock train. Two quasistable interaction modes were observed alternating between the top and bottom walls of the small-curvature isolator. The large-scale separations that are frequently encountered near the bottom wall of large-curvature isolators occur when the shock train is steadily interacting with a right-running shock. Investigation of the intrinsic flow mechanism of the self-excited and forced oscillations of a shock train subjected to background waves by Hou *et al.* [42,43] resulted in the proposal of three self-excited oscillation modes: top-large-separation, bottom-large-separation, and transition, and two forced oscillation modes: type I and type II, with the much larger oscillation range of type II significantly contributing to the stability of a working engine. Wang *et al.* [44,45] also used an upstream wedge to generate background waves and capture the motion

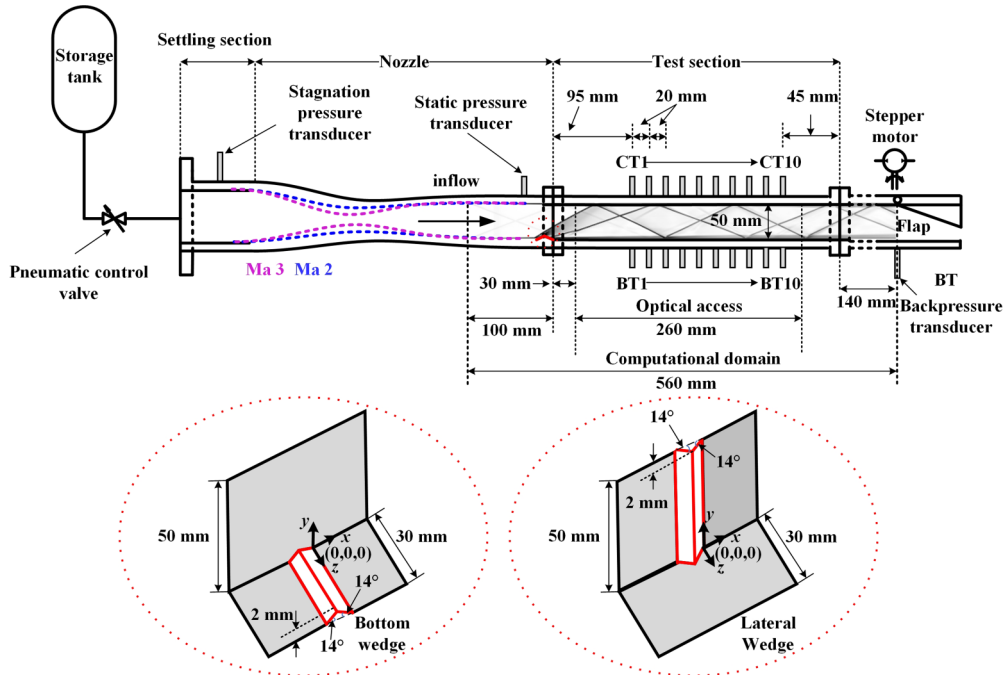


FIG. 2. Schematic diagram of the experimental setup.

behavior of the shock train at different positions by arranging pressure sensors in the mainstream and corner areas. High-speed schlieren with different knife edges was used to clearly demonstrate the structure of the shock train in a vertical flow cross section. The results indicated that the STLS is more three-dimensional at an incoming Mach number of 2.70 than it is under an incoming Mach number of 1.85. The closer the downstream disturbance to the STLS, the earlier the STLS moves.

Most studies are only concerned with the behavior of shock trains that form in the same plane as the background wave. However, shock trains present strong three-dimensional characteristics when associated with background waves, and it is therefore necessary that information on other planes is obtained via experiment or numerical simulation. For this reason, unlike our previous studies, this study is aimed at gaining flow-field information for the plane perpendicular to the background wave by mounting a wedge on the sidewall and visualizing the resulting flow via schlieren imaging, while also accurately depicting the three-dimensional structure of the shock train by numerical simulation. Steady and unsteady behaviors are revealed against the background wave of the shock train, providing a reference for the safe and stable operation of the ramjet engine. The overall organization of this paper is as follows. The operational parameter settings of the supersonic wind tunnel, flow-field visualization, and pressure measurement techniques are introduced in Sec. II. The numerical methods and their validity verification are outlined in Sec. III. The influence of the wedge installation position and incoming Mach number on the evolution of the background wave is discussed in Sec. IV A. The experimental structures of the shock train in different cases are presented in Sec. IV B. The dynamic characteristics of a shock train with a background wave are analyzed using the trajectory of the STLS and the static wall pressure in Sec. IV C, and the three-

dimensional steady structure of the shock train is described in Sec. IV D. Finally, the conclusions are summarized in Sec. V.

II. EXPERIMENTAL SETTING

A. Experimental conditions

The experiments were conducted in a direct-connect supersonic wind tunnel at the Harbin Institute of Technology. As shown in Fig. 2, incoming air was supplied from a storage tank with a volume of 10 m^3 at a pressure of 13 MPa. Two types of nozzles with nominal Mach numbers of 2 and 3 were placed upstream of the test section. The actual parameters at the entrance of the test section were obtained using a static-pressure transducer located at the nozzle outlet. The incoming Mach numbers at the test section were 1.85 and 2.70, the incoming total pressures were 0.29 and 0.63 MPa, and the incoming total temperature was 287.15 K. Other specific parameter information is provided in Table I. The width, height, and length of the test section were 30, 50, and 320 mm, respectively.

In an operating scramjet engine, the initial deceleration and pressurization of the incoming flow occur at the inlet, providing a proper combustion environment for the downstream combustion chamber. This process is accomplished via the formation of an incident shock and its reflected shocks, which are denoted background waves. To model the same operating environment, a wedge is often used in wind-tunnel experiments to generate background waves, allowing exploration of their coupling with the shock train. The same settings were used in this study. The angle of the wedge was 14° with a height of 2 mm. The effect of the different arrangements on the motion of the shock train was analyzed by setting up wedges at the bottom and lateral of the wall at the entrance of the test section, respectively.

A rotatable flap was installed downstream of the test section to create a shock train in the flow field. This flap, with an

TABLE I. Incoming flow parameters.

Case	Incoming Mach number M_∞	Incoming total pressure P_0 (MPa)	Incoming static pressure P_∞ (Pa)	Incoming total temperature T_0 (K)	Incoming static temperature T_∞ (K)	Incoming boundary-layer thickness δ_∞ (mm)	Ratio of wedge height to boundary-layer thickness	Back pressure ratio range	Wedge position
I	1.85	0.29	47 019.12	287.15	170.47	2.12	0.94	4–5.5	Bottom
II	1.85	0.29	47 019.12	287.15	170.47	2.12	0.94	4–5.5	Lateral
III	2.70	0.63	27 200.24	287.15	116.82	2.17	0.92	4–8	Bottom
IV	2.70	0.63	27 200.24	287.15	116.82	2.17	0.92	4–8	Lateral

angle resolution of 0.006° , is driven by a stepper servomotor to achieve throttling. The linear rotation of the flap corresponds to the linear increase in the backpressure, as shown in Fig. 3. The flap angle was observed to increase from 13.4° to 17.8° and 15.2° to 22.6° over a period of 19 s when subjected to incoming Mach numbers of 1.85 and 2.70, respectively. Four working conditions were investigated, denoted cases I–IV, with each condition repeated five times.

B. Wall static pressure measurements and high-speed schlieren

High-frequency wall-pressure measurements were used to quantify the dynamic oscillation characteristics of the shock train. As seen in Fig. 2, a stagnation pressure transducer was installed in the settling section and a static pressure transducer was placed at the nozzle outlet to obtain the incoming static pressure. A backpressure transducer was installed 140 mm from the test section to determine the backpressure and 20 high-frequency pressure transducers ranging from 0–100 kPa and an effective response frequency of approximately 20 kHz were arranged at 20-mm intervals on the ceiling and bottom walls within the test section. The transducers on the upper wall were denoted CT1 to CT10 and those on the lower wall were denoted BT1 to BT10. Details of the arrangement can be seen in Fig. 4. After calibration, the pressure transducers exhibited a nonlinear error of 0.1% full scale (F.S.), a repeatability error of 0.1% F.S., and a comprehensive accuracy of 0.1% F.S. The IOtech 6220 voltage measurement module with a cutoff frequency of >17 kHz was used to record signals at a sampling frequency of 10 kHz.

A Z-type reflective schlieren system, which includes a light source, condenser lens, slit, two spherical reflectors, a knife edge, and a high-speed camera (Photron V12) was used to capture the evolution of the shock train. The light propagation

path is shown in Fig. 5. The frame rate of the high-speed camera is 1000 fps and the exposure time is 250 μ s. The type of knife edge is adjustable and a vertical knife edge is used here. For further details, please refer to our previous studies [44].

III. NUMERICAL METHODS

Current well-known numerical methods include DNS, LES, and Reynolds-averaged Navier-Stokes Simulation (RANS). In contrast to the first two methods, RANS is widely used in engineering research because of the limited computational resources that are required due to its avoidance of solving flow structures on all scales. Recent studies [46] have revealed that steady RANS can capture the three-dimensional structure of a shock train and shock wave–boundary layer interaction.

In this study, the commercial software FLUENT was used to solve the three-dimensional compressible RANS equations. It is a steady, density-based, and implicit flow solver that is based on the finite-volume method. In the spatial discretization of N-S equations, the convective term is solved using a second-order upwind scheme and the turbulent kinetic energy and specific dissipation rate are determined using a first-order upwind scheme. The advection upstream splitting method is used to deal with shock-related numerical oscillations, producing a high-resolution flow field. The fluid is treated as a single-species ideal gas. The specific heat is determined using the piecewise polynomial method and the viscosity is calculated using Sutherland’s formula. The solution is regarded convergent when the residual drops by more than three orders of magnitude to its minimum and the difference between the calculated inflow and outflow mass fluxes falls below 0.001 kg/s.

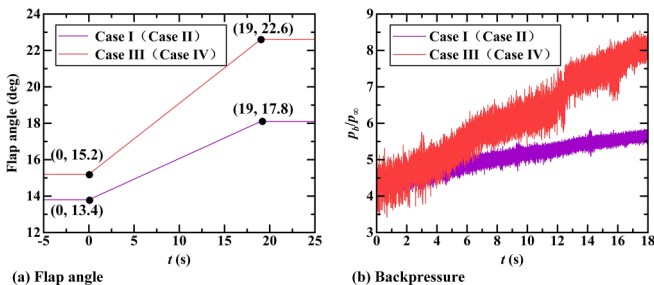


FIG. 3. Variation in the (a) flap angle and (b) corresponding backpressure over time.

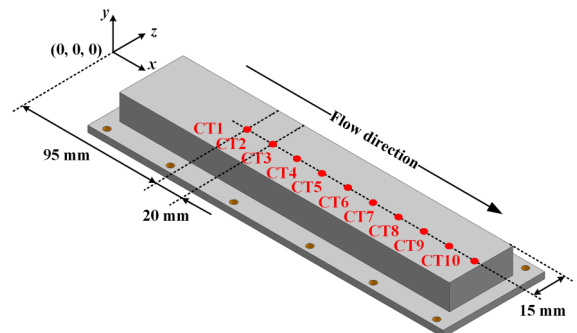


FIG. 4. Arrangement of wall-pressure transducers.

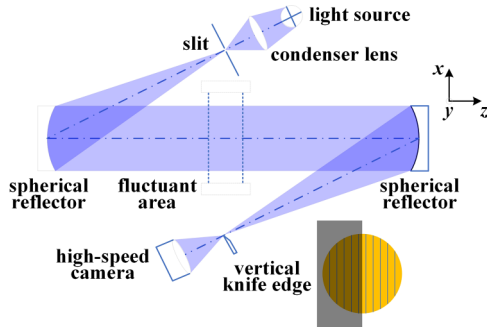


FIG. 5. Reflective schlieren system and corresponding knife-edge type.

The computational domain and boundary-condition settings of the flow field are illustrated in Fig. 6. The inlet plane at $x = -100$ mm was set as the pressure far field and the outlet plane at $x = 460$ mm as the pressure outlet in the streamwise direction. The boundary condition for the wall was set to a nonslip adiabatic condition. The entrance section was primarily designed to allow the development of a turbulent boundary layer of particular thickness at the entrance of the isolator section. The isolator section was set to a length of 320 mm for consistency with the experimental section. Wedges were mounted on the bottom and lateral walls at the origin of the isolator entrance to generate background waves running in different directions. The lengths of the two wedges, 30 and 50 mm, differed because of the unequal widths and heights in the experiments. However, the two wedges

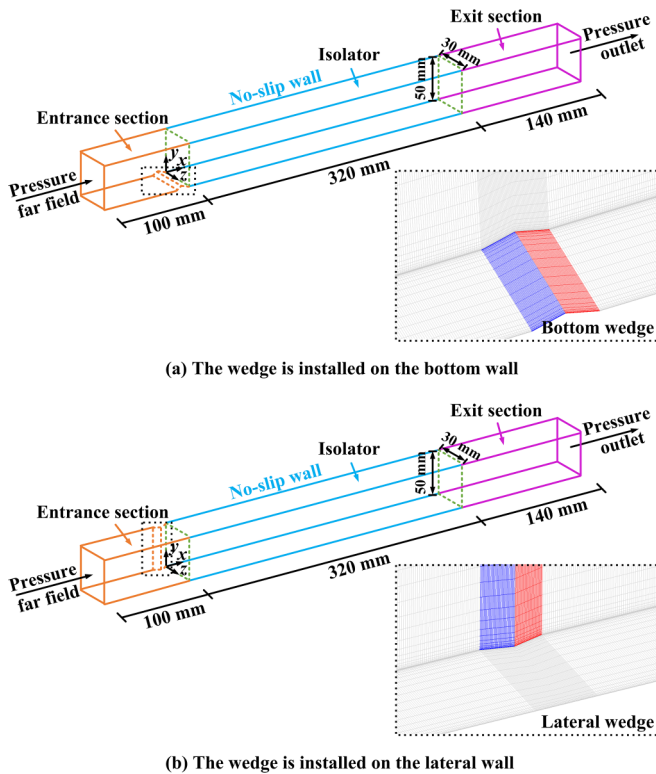


FIG. 6. Schematic of the computational domain and boundary condition. The partial model grids are depicted in the lower-right inset of each subfigure.

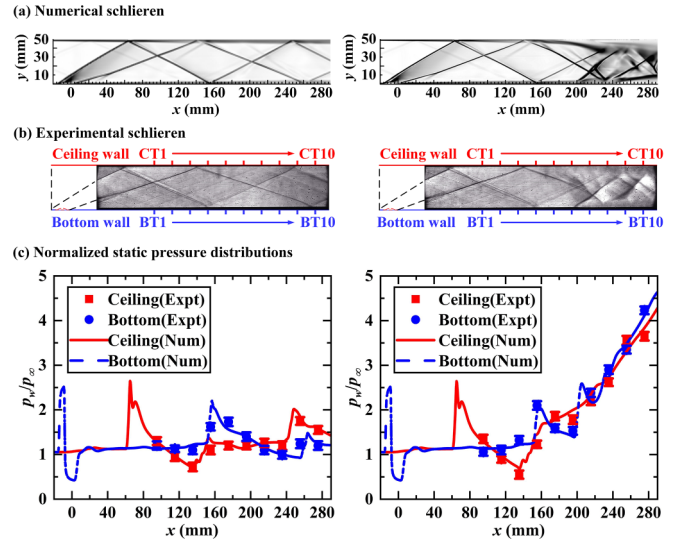


FIG. 7. Comparison of experimental and numerical schlieren and pressure distribution results with and without a shock train.

were of the same widths and heights, allowing simultaneous consideration of the effects of different background-wave orientations and the aspect ratios on the shock train. As illustrated in Table II, three grid scales were considered: coarse mesh (11.34×10^6), fine mesh (20.16×10^6), and dense mesh (26.88×10^6). To save computational resources while ensuring computational accuracy, a medium-scale grid (20.16×10^6) was selected for calculation.

Figure 7 shows the comparative results of the flow field and pressure distribution for an incoming Mach number of 2.70 obtained via experiment and numerical simulation. Numerical schlieren was obtained using a vertical knife edge. As shown in Figs. 7(a) and 7(b), both the experiments and numerical simulations accurately captured the structure of the shock wave, expansion wave, and separation bubble, regardless of whether a shock train formed in the flow field. In addition, the pressure distributions obtained in the experimental and numerical results agree well, with $<2\%$ error, as seen in Fig. 7(c). These results demonstrate the accuracy of the proposed numerical method.

IV. RESULTS AND DISCUSSION

A. Variation of background waves in association with wedge position and incoming Mach number

Prior to analyzing the coupling interaction between the background wave and the shock train, the development of the background wave requires clarification. The high-speed schlieren equipment used in the wind-tunnel experiments can obtain the evolution of the flow field in the spanwise direction. However, the pressure data obtained from the pressure transducers are discrete and cannot continuously characterize the visualized flow field. Consequently, numerical simulation is performed to analyze the evolution of the background wave.

Figure 8 illustrates the density-gradient contours of the background wave in two central planes ($y = 25$ mm and $z = 15$ mm) and the pressure distribution at the four walls in case I, in which the flow field is through-flow and no

TABLE II. Grid resolution.

Computational domain	Entrance section			Isolator			Exit section		
	N_x	N_y	N_z	N_x	N_y	N_z	N_x	N_y	N_z
Coarse	150	150	90	480	150	90	210	150	90
Fine	150	200	120	480	200	120	210	200	120
Dense	200	200	120	640	200	120	280	200	120

shock train forms. The wall-pressure profile is normalized to the incoming static pressure. The $y = 0$ mm plane is the bottom wall, $y = 50$ mm is the ceiling wall, $z = 0$ mm is the left wall, and $z = 30$ mm is the right wall. The corresponding density-gradient diagram shows that when the wedge is mounted on the bottom wall, the airflow decelerates and pressurization occurs mainly in the vertical plane, with two incident shocks (i_1 and i_2) generated at the leading and trailing edges of the wedge, respectively. Owing to the intense shock wave–boundary layer interaction, the incident shock (i_1) is reflected at the ceiling wall, which in turn induces a reflected shock (i_3) and a reattachment shock (i_4) at reflection point T_1 , where a separation bubble forms. The reflected shocks of incident shocks i_1 and i_2 are observed to merge after reflection point T_5 , combining to form a single shock. A total of ten reflection points (T_1 – T_5 and B_1 – B_5) are presented on the ceiling and bottom walls over a streamwise distance of -30 to 290 mm. In addition, in terms of the density-gradient schlieren in the horizontal central plane ($y = 25$ mm), the background wave exhibits distinctly two-dimensional characteristics, with a symmetric structure in the horizontal flow direction.

Extracting the normalized pressure at the four walls allows elucidation of the adverse pressure gradient in the region of

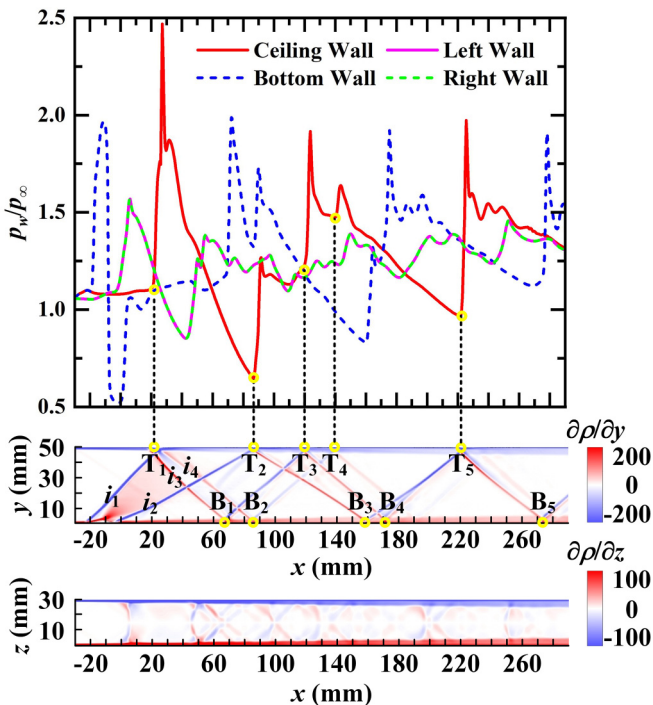


FIG. 8. Normalized wall-pressure distribution and density-gradient diagrams of the two central planes in case I.

the shock wave–boundary layer interaction near the reflection point, $\partial p/\partial x > 0$, while the favorable pressure-gradient region lies between the two reflection points at $\partial p/\partial x < 0$. Comparison of the pressure distribution in the four planes indicates that the wall-pressure gradient is higher in the longitudinal cross section (ceiling and bottom walls) than in the transverse cross section (left and right walls), with distinct peaks and troughs. The wall-pressure profiles of the left and right walls are almost overlapping, and except for a large pressure gradient near the wedge, the pressure varies very flatly downstream.

Figure 9 shows the density-gradient contours of the two central planes ($y = 25$ mm and $z = 15$ mm) in the other three cases. In case II, the incident shocks that are generated by the airflow passing through the wedge are reflected in the transverse cross section. Since the width of the computational

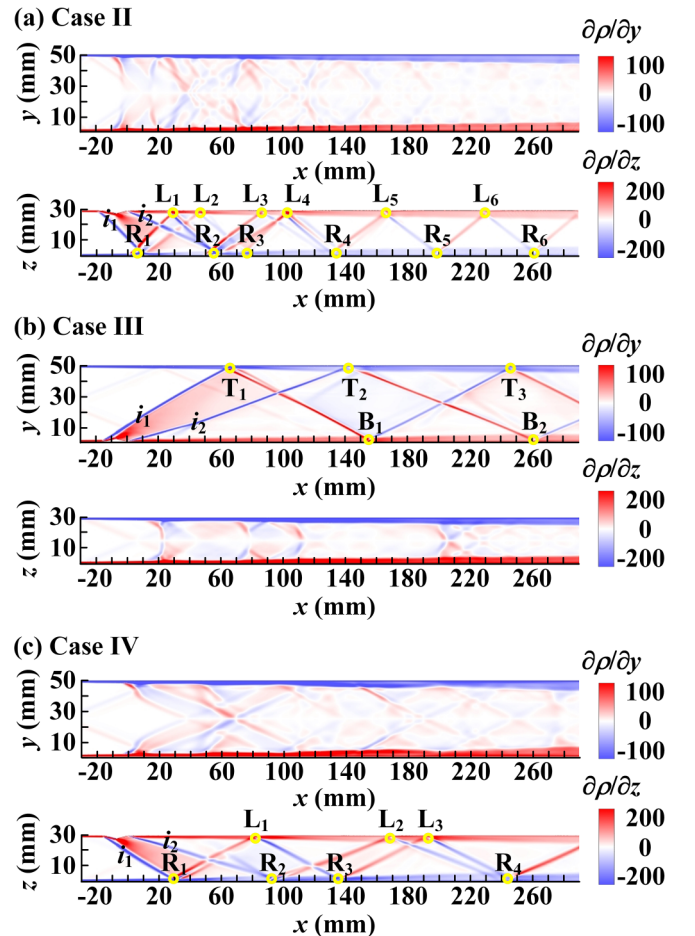


FIG. 9. Structure of the background wave in two central planes in (a) case II, (b) case III, and (c) case IV.

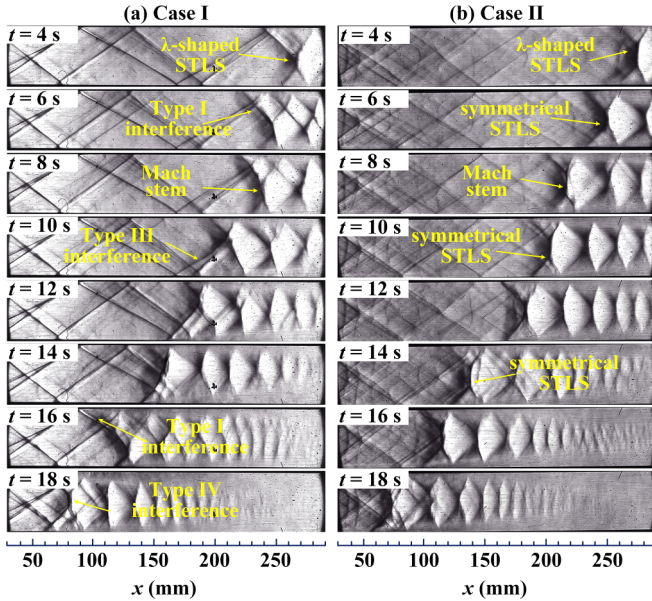


FIG. 10. Schlieren images of shock train from $t = 4$ s to $t = 18$ s in (a) case I and (b) case II.

domain is smaller than the height, the space required for the incident shock to undergo reflection decreases, which means that more reflected shocks form over the flow distance of -30 to 290 mm. In addition, the reflected shocks of incident shocks i_1 and i_2 are merged into a single shock at the reflection point R_4 earlier.

As the incoming Mach number increases, the shock angles of incident shocks i_1 and i_2 decrease, and the locations of reflection points T_1 and L_1 move further downstream, as shown in Figs. 9(b) and 9(c). Comparison of cases I and III or cases II and IV reveals that the distance between reflection points continues to increase and that the number of reflection points decreases as the incoming Mach number is increased. In both cases, strong two-dimensional features are observed in the background wave, which displays a symmetric structure in the plane perpendicular to the reflection of the incident shock.

B. Experimental morphology of the shock train

1. Incoming Mach number is 1.85

To explore the evolutionary behavior of the shock train in association with the background wave, the motion of the shock train in the vertical central section is obtained experimentally using schlieren visualization. Cases I and II, with an incoming flow Mach number of 1.85, are analyzed first. The structure of the shock train with a vertical knife edge from $t = 4$ s to $t = 18$ s is shown in Fig. 10.

As seen in Fig. 10(a), the morphology of the shock train is highly enriched and diverse when the shock train is in the same plane as the background wave. As the backpressure increases, the shock train gradually moves upstream and its morphology changes to comprise both symmetric and asymmetric λ -shaped structures. The interaction modes of the shock train and the background wave can be divided into four types: I and III, in which the shock train exhibits an asymmetric pattern, and II and IV, in which the shock train is symmetric. As shown

in Fig. 11, the intrinsic flow mechanisms are in accordance with the following conditions. When the background wave interacts with the STLS on only one side, a shock-shock interaction occurs, intensifying the corresponding flow separation and increasing the scale of the separation bubble. These factors lead to the formation of interaction patterns I and III, with large separation on one side of the flow field and small separation on the other; in contrast, when the background wave interacts with the Mach stem of a λ -shaped shock train or interferes bilaterally with the STLS on both sides, flow equilibrium is maintained, with separation bubbles of identical size on both sides and a symmetric shock train.

The experimental schlieren structures of a shock train with the wedge mounted on a lateral wall are shown in Fig. 10(b). In this case, the flow field displays the morphology of the shock train in the plane perpendicular to the background wave. In this situation, as the backpressure increases, the shock train adopts a symmetric structure with the flow separation maintaining the equilibrium on both sides of the ceiling and bottom walls.

To demonstrate the symmetric nature of the STLS in case II, 2000 data points are selected and the mean and rms pressure profiles for the ceiling and bottom walls are calculated at $t = 10$ s and $t = 14$ s, as shown in Fig. 12. The mean pressure at each transducer position is normalized using the incoming static pressure. An uncertainty of 5% is indicated by the error bars. As shown in Figs. 12(a) and 12(b), the presence of the shock train leads to a significant increase in the mean pressure, with the rms pressure reaching its maximum value at the STLS, after which it gradually decreases to match the pressure level of the separated flow downstream. The stream-wise length of the STLS is essentially the same, at 22.23 and 22.31 mm. The pressure profiles on the ceiling and bottom walls are almost overlapping, regardless of the mean or rms pressure. These results indicate that the shock train can in this case be regarded as two dimensional, with the influence of the background waves dominating the shock train.

2. Incoming Mach number is 2.70

When the incoming Mach number is increased from 1.85 to 2.70, the morphology of the shock train changes from λ shaped to X shaped. Figure 13 shows the experimental schlieren images obtained during the upstream movement of the shock train in cases III and IV. In case III, the X-shaped STLS undergoes a transition between an asymmetric and symmetric structure, which is mainly characterized by its interaction with the background wave. The distinctive shock-induced separations are classified into three patterns: two asymmetric (types V and VII) and one symmetric (type VI), as shown in Fig. 14. The type V (type VII) interference occurs when the background wave and shock train cross at a large separation bubble at the bottom (top) region of the wall. In contrast, the two shock feet of the STLS interact with the background waves on both sides, resulting in the same degree of flow separation at the top and bottom walls. In addition, a rapid upstream movement of the STLS is observed in the flow field when the STLS passes the reflection point at $t = 16$ s to $t = 18$ s.

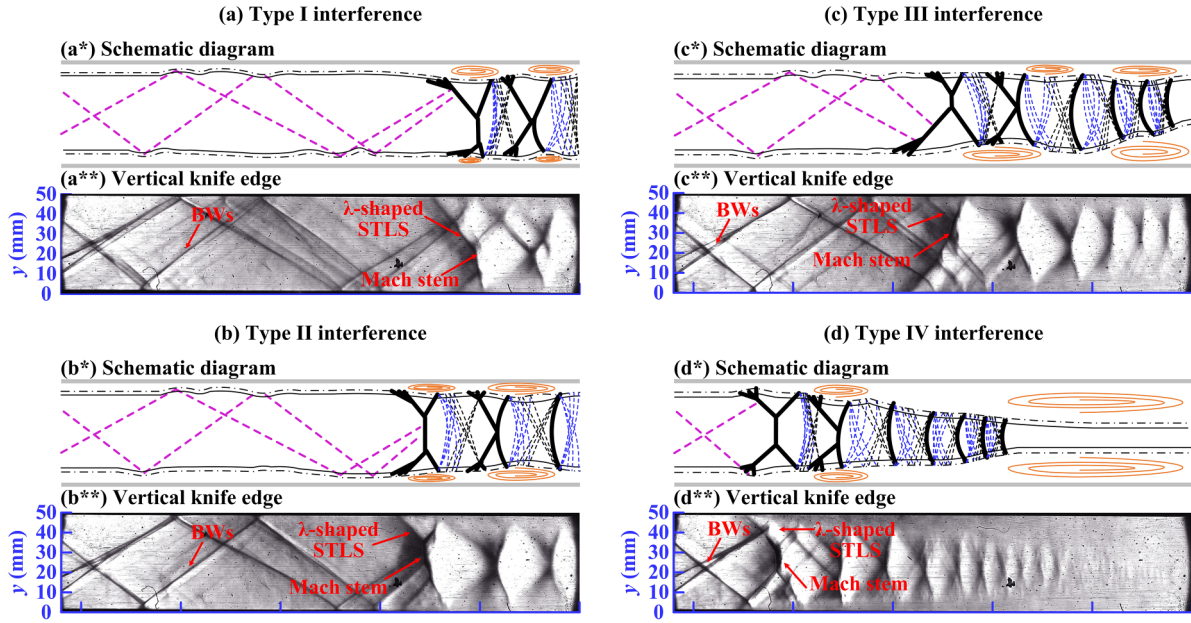


FIG. 11. Four typical interaction modes of shock train with background waves (BWs) in case I.

Schlieren visualization of the shock train in case IV is shown in Fig. 13(b). The morphology of the shock train differs from that in case II in that the STLS is no longer symmetric during forward movement. From $t = 4$ s to $t = 10$ s, the STLS skews toward the ceiling wall, and the overall extent of the separated flow in the bottom wall increases. However, after a rapid movement of the shock train that occurs from $t = 10$ s to $t = 12$ s, the STLS suddenly becomes symmetric in structure, and remains in this form until its disappearance.

Figure 15 shows the mean and rms pressure distributions of the flow field at $t = 8$ s and $t = 14$ s in case IV. The mean pressures on the ceiling and bottom walls are consistent with those of an asymmetric STLS ($t = 8$ s) in the upstream attached

region, whereas a large difference is observed in the regions at which the STLS is separated. The points of extreme rms pressure are at different locations on the ceiling and bottom walls, indicating enhanced three dimensionality of the shock train. In contrast, under a symmetric STLS ($t = 14$ s), the mean and rms pressures of the ceiling and bottom walls coincide, and the streamwise length of the STLS near the bottom wall at $t = 8$ s is approximately 1.5 times that at $t = 14$ s.

C. Dynamic behavior of the shock train

In this section, the dynamic properties of the shock train are analyzed using the trajectories of the STLS and the

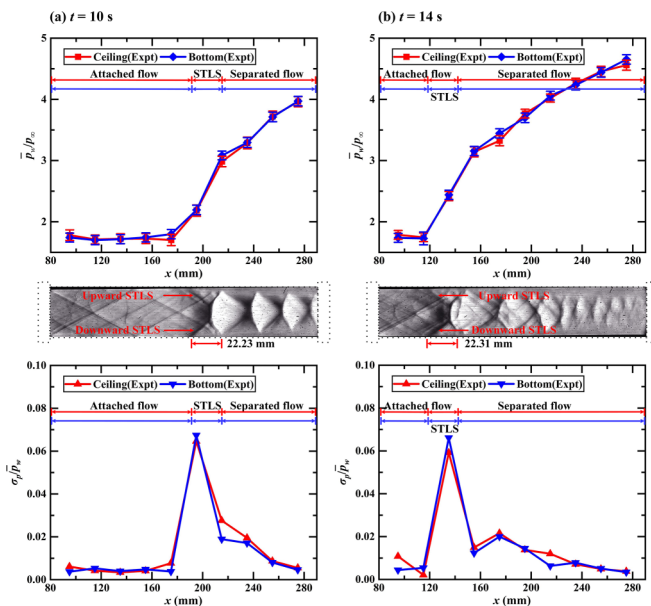


FIG. 12. Normalized mean and rms pressure profiles at (a) $t = 10$ s and (b) $t = 14$ s in case II.

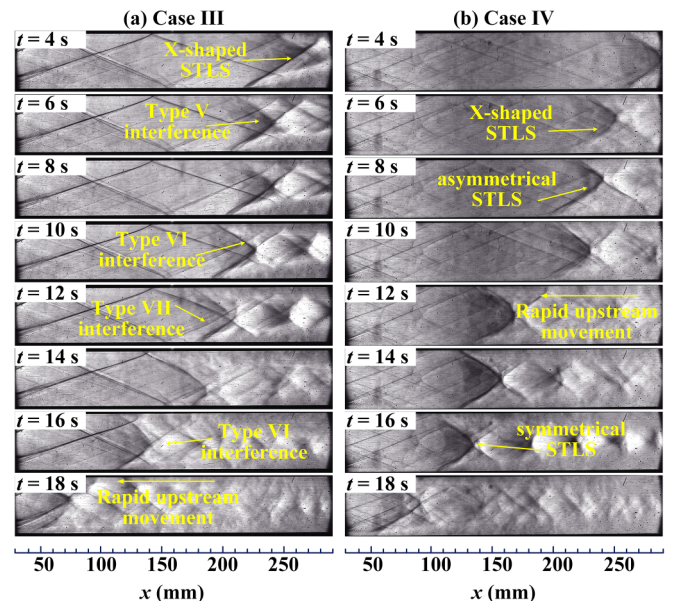


FIG. 13. Schlieren images of shock train from $t = 4$ s to $t = 18$ s in (a) case III and (b) case IV.

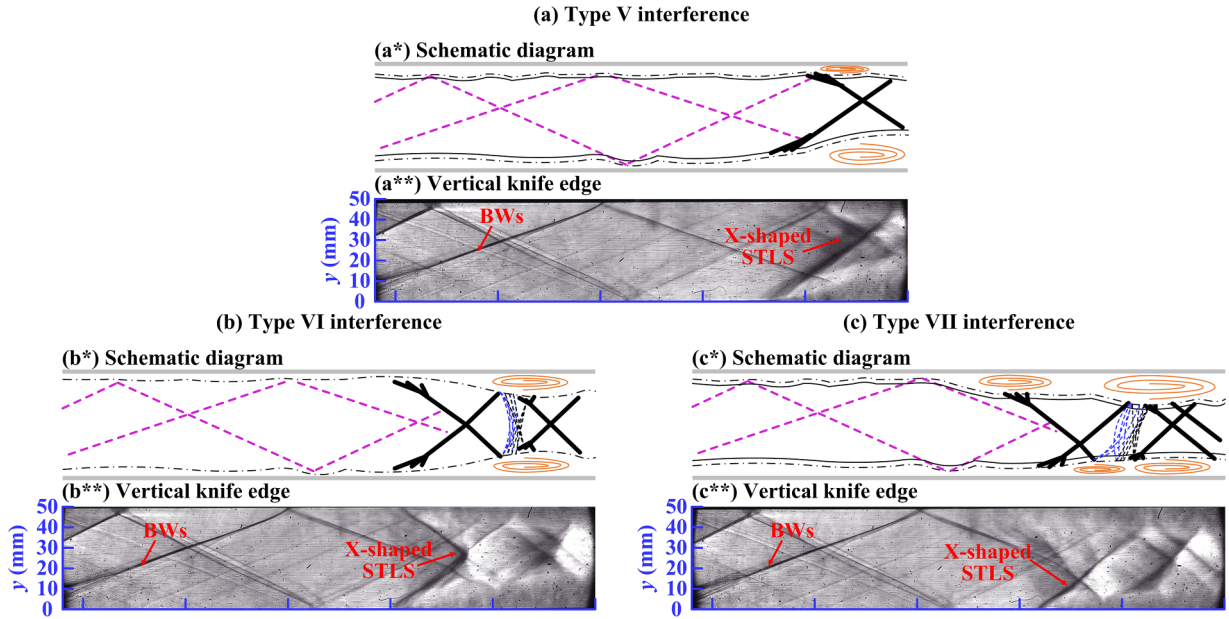


FIG. 14. Three interaction modes of shock train with BWs in case III.

wall-pressure histories obtained from the experimental measurements. The STLS trajectory is calculated from 50-frame intervals. Six pressure transducers on the ceiling (CT5, CT7, and CT9) and bottom (BT5, BT7, and BT9) walls are selected to record the transient pressure information in each case.

Figure 16 shows the trajectory variations of the STLS at the ceiling and bottom wall during the upstream movement of the shock train in cases I and II. In case I, the trajectory variations at the ceiling and bottom walls clearly reveal mode conversion in the interaction between the shock train and background wave. Before $t = 9.5$ s, the trajectory at the ceiling wall is always upstream of that at the bottom wall, after which the interaction mode of the background wave and the shock train

switch from type I to type II and then to type III. The duration of type II is transitional, and the interaction pattern returns to type I after $t = 14$ s. Comparatively, in case II, the trajectories of the STLS of the ceiling and bottom walls overlap, again demonstrating the symmetric structure that is maintained by the STLS during operation.

The oscillation magnitude of the STLS trajectory intensifies significantly as the incoming Mach number increases. The trajectories of the STLS in cases III and IV are shown over time in Fig. 17. In case III, the interaction pattern between the shock train and background wave is initially type V, with the STLS positioned upstream at the bottom wall. The shock train then changes from asymmetric to symmetric, with almost the same trajectories observed at the ceiling and bottom wall. However, this stage lasts for only a very short period, and the STLS at the ceiling wall moves rapidly upstream, leading to a type VII interaction mode. The rapid movement of the shock train is clearly observed in the STLS trajectory at approximately $t = 11$ s in case IV. Prior to $t = 11$ s, the trajectories of the STLS do not coincide at the ceiling and bottom walls. However, these trajectories are the same after the observed rapid STLS movement, indicating that the shock train is symmetric at this time.

Figures 18 and 19 show the pressure-time histories and power spectral density (PSD) contours for all experimental cases. The oscillation characteristics of the shock train in cases I and II are compared first. As seen in Figs. 18(a) and 18(b), the transient pressure variations clearly delineate the morphological transformation of the shock train. The difference in the pressure distribution between the top and bottom walls is evident when the STLS is asymmetric. However, no significant difference in the pressure distribution at the top and bottom walls is observed when the STLS is symmetric. When the shock train is in the same plane as the background wave (case I), the STLS sweeps across the BT9 transducer at $t = 2-6$ s, and the pressure oscillation energy oscillates in the range 5–200 Hz, decreasing to 5–60 Hz when the STLS

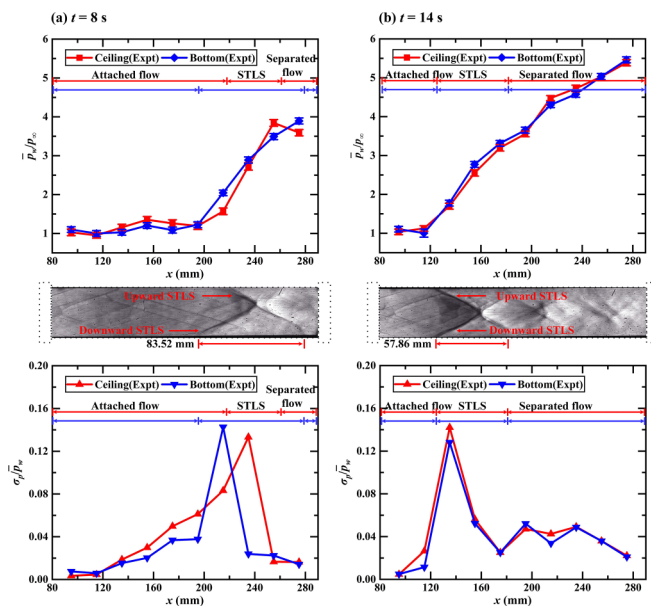


FIG. 15. Normalized mean pressure and rms pressure profiles at (a) $t = 8$ s and (b) $t = 14$ s in case IV.

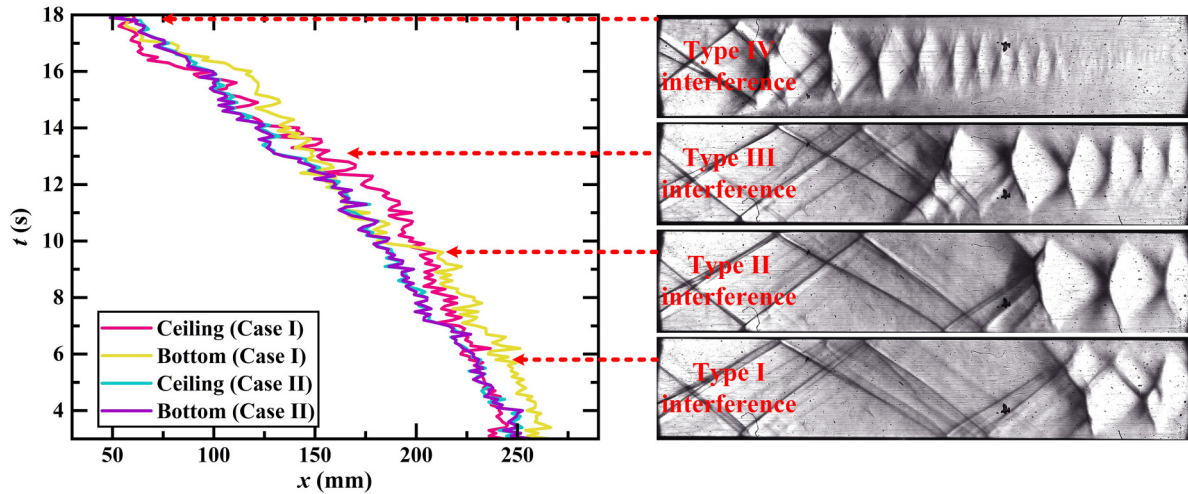


FIG. 16. Trajectories of the STLS over time in cases I and II.

moves upstream to BT7. These results indicate that the further the STLS is upstream, the weaker the degree of self-excited oscillation. The range of the pressure oscillation energy for the shock train as it crosses BT9 is also approximately 5–200 Hz in case II; however, it decays more rapidly during the upstream movement in this instance.

As shown in Figs. 19(a) and 19(b), the magnitude of the pressure oscillations rises as the Mach number increases. In case III, the pressure oscillation energy varies below 1000 Hz and is primarily concentrated at 10 Hz when the STLS is near BT9 at $t = 2-4$ s. When the shock train moves upstream at $t = 8-12$ s, the pressure oscillation energy downstream of the shock train is primarily concentrated at 100 Hz, which is attributed to the fact that B_2 , the reflecting point of the background wave, is also oscillating near BT9 at this point. In case IV, the rapid forward movement of the shock train at $t = 11$ s is accompanied by gradual consistency in the instantaneous pressure distributions on the top and bottom walls, regardless of position. The oscillation range of the pressure oscillation energy is below 1000 Hz when the STLS oscillates near BT9 at $t = 2-6$ s. Similarly, the pressure oscillations caused by the shock train gradually weaken as the shock train moves upstream.

D. Three-dimensional steady structure of the shock train

Case IV is employed to recognize and analyze the three-dimensional morphological structure of the shock train. The structure of the shock train obtained from the three-dimensional steady RANS calculations at a backpressure ratio of 7 is shown in Fig. 20, and corresponds to the experimental results describing the shock train following its rapid movement. The velocity contours for different cross sections are displayed along with the pressure gradient and velocity isosurfaces. The three-dimensional structure of the background wave and shock train is represented using the pressure gradient isosurface $\partial p/\partial x = 1 \times 10^6$ Pa/m, with the velocity isosurface $u = -1$ m/s expressing the separation region. In agreement with the experimental observation, the STLS is symmetrical in the vertical central plane ($z = 15$ mm) of the flow field at this point, as demonstrated by the fact that the velocity contours are identical in planes $y = 5$ mm and $y = 45$ mm (or $y = 15$ mm and $y = 35$ mm) of the horizontal cross section, with all flow fields comprising symmetric structures in the velocity contours describing the different vertical cross sections. Three separation bubbles have formed in the STLS: one at the corner between the ceiling and the right wall, one at the center of the right wall, and one at the corner between

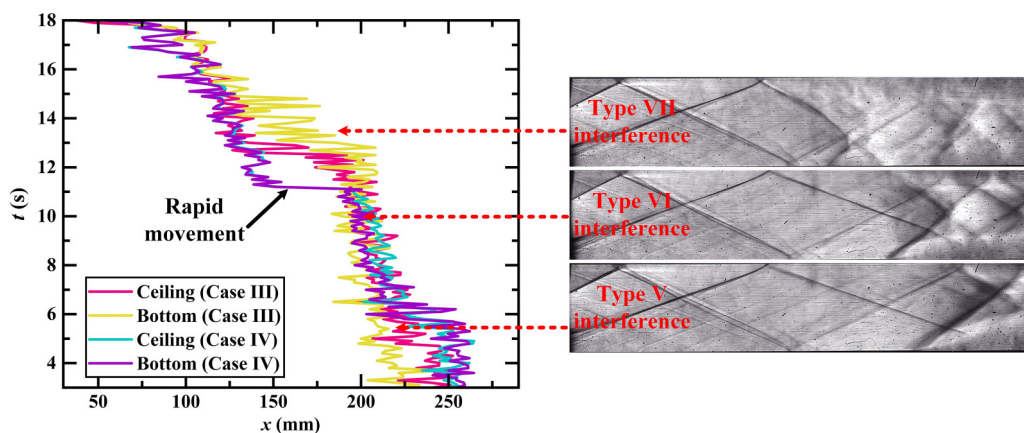


FIG. 17. Trajectories of the STLS over time in cases III and IV.

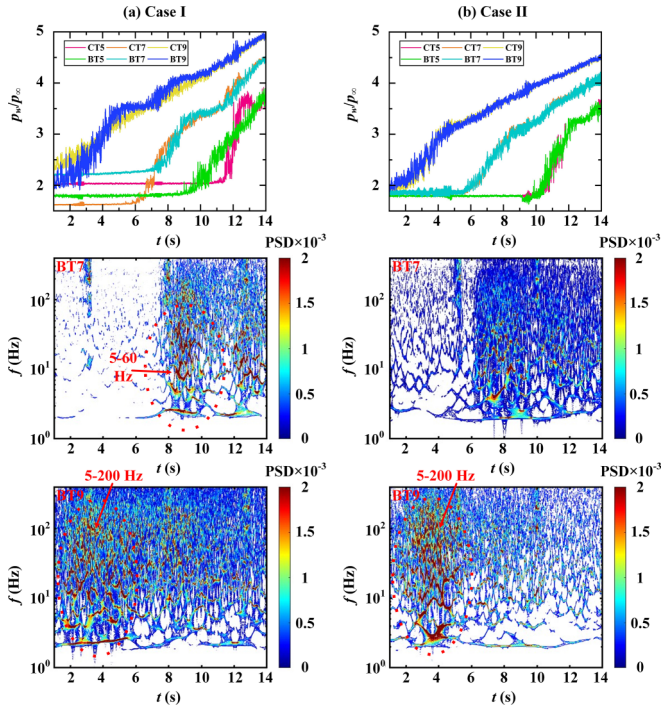


FIG. 18. Pressure-time histories and PSD contours in cases I and II.

the bottom and the right wall. Simultaneously, two larger separation regions that have formed at the junction between the left wall and the ceiling and at the bottom wall extend downstream of the flow field.

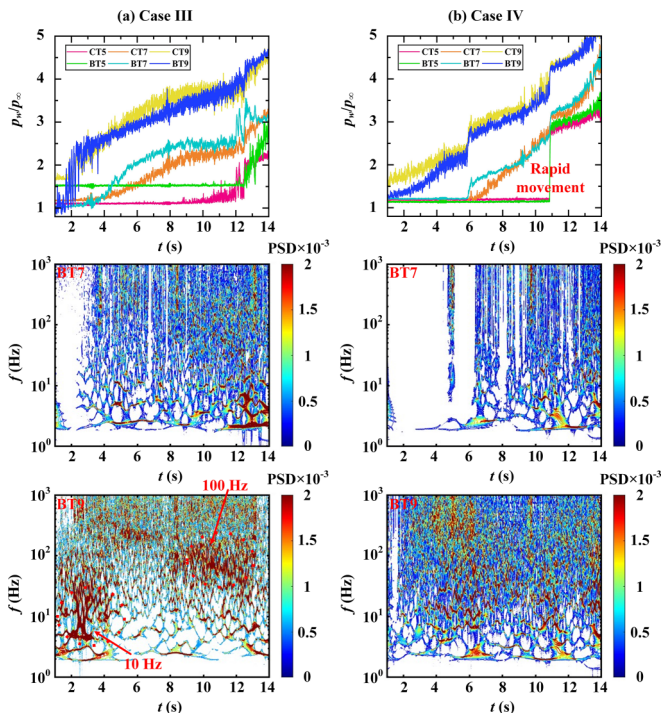


FIG. 19. Pressure-time histories and PSD contours in cases III and IV.

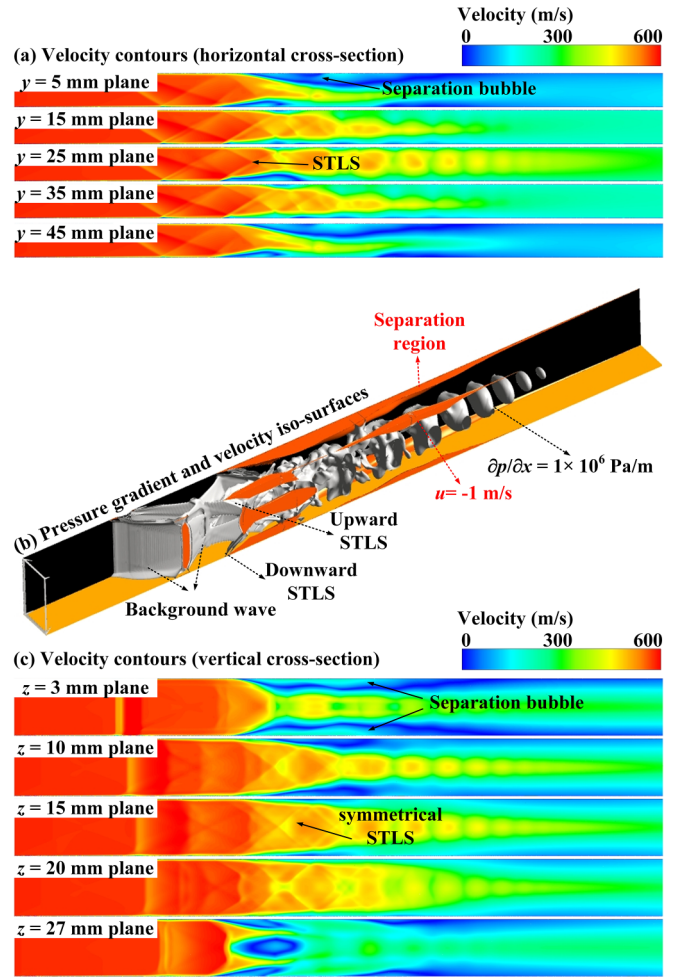


FIG. 20. Velocity contours showing (a) horizontal and (c) vertical cross sections in case IV. (b) Pressure gradient and velocity iso-surfaces in case IV.

The streamline distributions of the ceiling and bottom walls and the x -wall shear-stress distributions in the different cross sections are presented in Fig. 21. The flow distributions on the ceiling and bottom walls are essentially identical and clearly capture the corresponding separation regions. A large separation region and two small separation regions are observed simultaneously on the ceiling and the bottom wall, with each showing shear-stress values of less than zero and a local minimum at the separation core. Similarly, the x -wall shear-stress distributions on the ceiling and the bottom wall are consistent, confirming symmetry for the shock train in the vertical cross section.

V. CONCLUSION

The purpose of this study was to investigate the effect of background waves traveling in different directions on the motion process of a shock train. The evolution of the shock train traveling both parallel and perpendicular to the flow compression of the background wave was observed in supersonic wind tunnels with incoming Mach numbers of 1.85 and 2.70. The generation of background waves in different directions was realized by installing wedges on the bottom and lateral walls

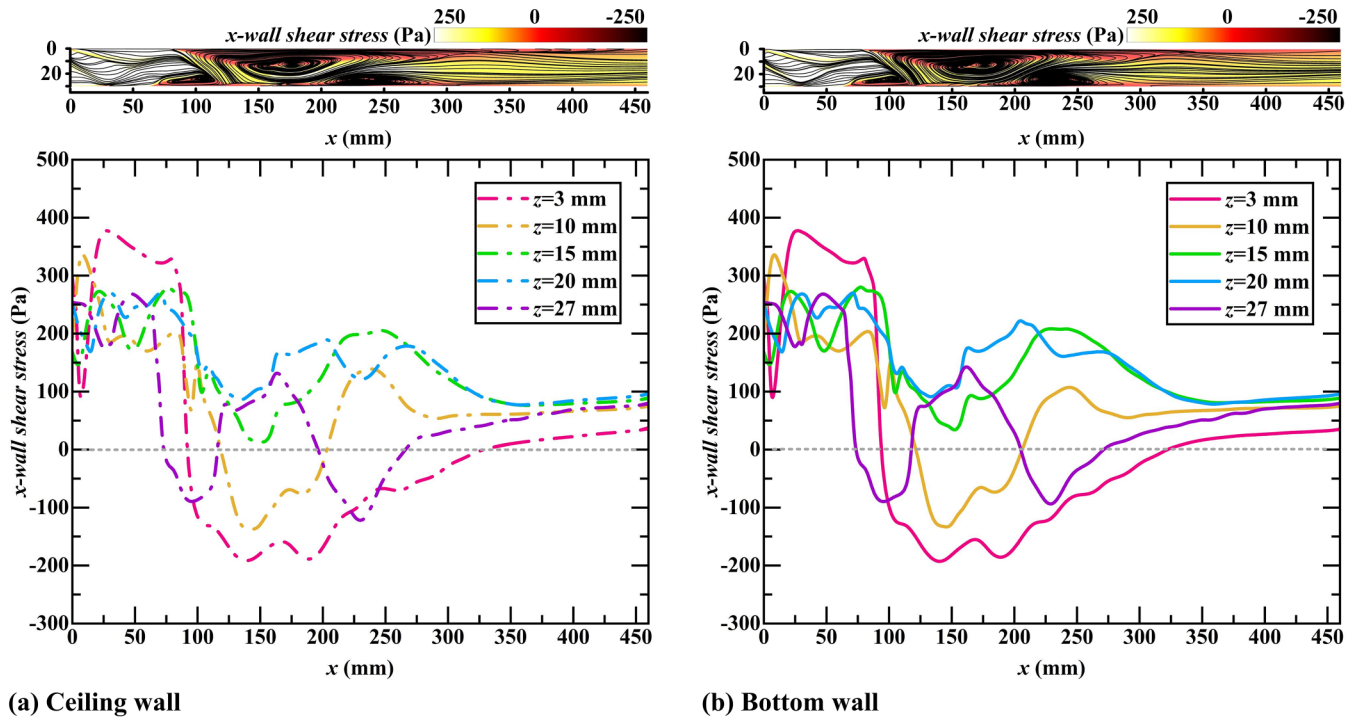


FIG. 21. Separation patterns and x -wall shear-stress distributions on the ceiling and bottom walls in case IV.

at the entrance to the isolator section. The three-dimensional structure of the shock train was depicted using the steady RANS numerical method, with the wall transient pressure and schlieren images used to record the dynamic characteristics of the shock train.

Both the installation position of the wedge and the variation in the incoming Mach number influence the formation of background waves. When the wedge is mounted on the bottom wall, the airflow decelerates and becomes pressurized in the vertical cross section with the incident shock reflected on the top and bottom walls; however, mounting the wedge on the sidewall results in the reflection of the incident shock on the sidewalls. Because the height of the computational domain is greater than the width, more reflected shocks are generated when the incident shocks are reflected at the sidewalls, and the reflected shocks of incident shocks i_1 and i_2 rapidly merge to form a single shock. The shock angle of the incident shock decreases as the Mach number increases, and fewer reflection points are established in the flow field. Nevertheless, in all cases, the background wave exhibits two-dimensional features.

The experimental schlieren images show the changes in the shock train morphology. The interaction modes of the background wave and shock train can be classified into four categories at an incoming Mach number of 1.85 and three categories at an incoming Mach number of 2.70 when the background wave and shock train are in the same flow cross section. However, the STLS always remains symmetric during its upstream motion when the background wave is perpendicular to the shock train at an incoming Mach number of 1.85. Furthermore, the STLS forms a three-dimensional and asym-

metric structure before rapid movement occurs at an incoming Mach number of 2.70. The mean and rms pressure distributions confirm the transformation of the STLS morphology.

As the incoming Mach number increases, the trajectory of the STLS indicates an intensification of the oscillation magnitude for the shock train. The PSD contours indicate that the pressure oscillation energy range of the shock train is not strongly dependent on whether the shock train is in the same compression plane as the background wave. The pressure oscillation energy range was 5–200 Hz at an incoming Mach number of 1.85, whereas it was below 1000 Hz at an incoming Mach number of 2.70. In all four cases considered in this study, the intensity of the pressure oscillations of the shock train decreased as the shock train moved upstream. Numerical steady-state calculations were used to ascertain the three-dimensional structure of the shock train in case IV. The velocity distributions in the different cross sections, as well as the wall shear-stress distributions at the ceiling and bottom walls, confirm the symmetric structure of the shock train in the vertical streamwise cross section. However, steady calculations fail to provide a reasonable explanation for why the STLS transforms from an asymmetric to a symmetric structure after rapid movement; thus, further exploration of this phenomenon is required in the future.

ACKNOWLEDGMENTS

This research work is supported by the National Natural Science Foundation of China (Grants No. 52125603, No. 12202122, and No. U2341240) and the China Postdoctoral Science Foundation (Grant No. 2023M730854).

- [1] J. T. Chang, N. Li, K. J. Xu, W. Bao, and D. R. Yu, Recent research progress on unstart mechanism, detection and control of hypersonic inlet, *Prog. Aerosp. Sci.* **89**, 1 (2017).
- [2] E. T. Curran, Scramjet engines: The first forty years, *J. Propuls. Power* **17**, 1138 (2001).
- [3] G. Choubey, Y. Devarajan, W. Huang, K. Mehar, M. Tiwari, and K. M. Pandey, Recent advances in cavity-based scramjet engine—a brief review, *Int. J. Hydrog. Energy* **44**, 13895 (2019).
- [4] K. R. Sekar, S. K. Karthick, S. Jegadheeswaran, and R. Kannan, On the unsteady throttling dynamics and scaling analysis in a typical hypersonic inlet–isolator flow, *Phys. Fluids* **32**, 126104 (2020).
- [5] H. B. Wang, Z. G. Wang, M. B. Sun, and H. Y. Wu, Combustion modes of hydrogen jet combustion in a cavity-based supersonic combustor, *Int. J. Hydrog. Energy* **38**, 12078 (2013).
- [6] S. M. Prabakar, C. Srikanth, and T. M. Muruganandam, Effect of Mach number on shock oscillations in supersonic diffusers, in *Proceedings of the 30th International Symposium on Shock Waves 1* (Springer, Cham, 2017), p. 257.
- [7] B. Morgan, K. Duraisamy, and S. K. Lele, Large-eddy simulations of a normal shock train in a constant-area isolator, *AIAA J.* **52**, 539 (2014).
- [8] A. Gillespie and N. D. Sandham, Shock train response to high-frequency backpressure forcing, *AIAA J.* **60**, 3736 (2022).
- [9] X. T. Tong, L. J. Yue, H. Chen, Q. F. Zhang, and C. M. He, Similarity analysis on two-dimensional hypersonic inlets unstart, *AIAA J.* **61**, 555 (2023).
- [10] B. Xiong, X. Q. Fan, Z. G. Wang, and Y. Tao, Analysis and modelling of unsteady shock train motions, *J. Fluid Mech.* **846**, 240 (2018).
- [11] L. Vanstone, J. Lingren, and N. T. Clemens, Simple physics-based model for the prediction of shock-train location, *J. Propuls. Power* **34**, 1428 (2018).
- [12] C. Fischer and H. Olivier, Experimental investigation of the shock train in an isolator of a scramjet inlet, in *Proceedings of the 17th AIAA International Space Planes and Hypersonic Systems and Technologies Conference* (American Institute of Aeronautics and Astronautics, San Francisco, California, 2011), p. 2220.
- [13] L. M. Edelman and M. Gamba, Structure of a Mach 2 shock train from experimental measurements, in *Proceedings of the AIAA Scitech 2020 Forum* (American Institute of Aeronautics and Astronautics, Orlando, FL, 2020), p. 1609.
- [14] Y. Ji, M. S. He, X. B. Huang, H. Q. Sheng, W. Wang, M. Y. Xie, and H. Liu, Influence of the rising rate of backpressure on the upstream motion characteristics of the shock train in a scramjet isolator, *Phys. Fluids* **35**, 041708 (2023).
- [15] L. H. He, H. Chen, L. J. Yue, Q. F. Zhang, and W. N. Wu, Interaction of a shock train with inherent isentropic waves in a curved isolator, *Phys. Fluids* **34**, 066106 (2022).
- [16] J. K. James and H. D. Kim, Oscillatory behaviors of multiple shock waves to upstream disturbances, *Phys. Fluids* **35**, 056113 (2023).
- [17] V. R. Petha Sethuraman, Y. Yang, and J. G. Kim, Low-frequency shock train oscillation control in a constant area duct, *Phys. Fluids* **34**, 016105 (2022).
- [18] J. L. Wagner, K. B. Yuceil, A. Valdivia, N. T. Clemens, and D. S. Dolling, Experimental investigation of unstart in an inlet/isolator model in Mach 5 flow, *AIAA J.* **47**, 1528 (2009).
- [19] R. Saravanan, S. L. N. Desikan, K. J. Francise, and R. Kalimuthu, Experimental investigation of start/unstart process during hypersonic intake at Mach 6 and its control, *Aerosp. Sci. Technol.* **103**, 106688 (2021).
- [20] P. J. Waltrup and F. S. Billig, Prediction of precombustion wall pressure distributions in scramjet engines, *J. Spacecr. Rockets.* **10**, 620 (1973).
- [21] P. J. Waltrup and F. S. Billig, Structure of shock waves in cylindrical ducts, *AIAA J.* **11**, 1404 (1973).
- [22] K. Matsuo, Y. Miyazato, and H. D. Kim, Shock train and pseudo-shock phenomena in internal gas flows, *Prog. Aerosp. Sci.* **35**, 33 (1999).
- [23] F. Gnani, H. Zare-Behtash, and K. Kontis, Pseudo-shock waves and their interactions in high-speed intakes, *Prog. Aerosp. Sci.* **82**, 36 (2016).
- [24] P. J. K. Bruce, H. Babinsky, B. Tartinville, and C. Hirsch, Experimental and numerical study of oscillating transonic shock waves in ducts, *AIAA J.* **49**, 1710 (2011).
- [25] B. Xiong, Z. G. Wang, X. Q. Fan, and Y. Wang, Response of shock train to high-frequency fluctuating backpressure in an isolator, *J. Propuls. Power* **33**, 1520 (2017).
- [26] B. Xiong, Z. G. Wang, X. Q. Fan, and Y. Wang, Experimental study on the flow separation and self-excited oscillation phenomenon in a rectangular duct, *Acta Astronaut.* **133**, 158 (2018).
- [27] R. Fiévet, H. Koo, V. Raman, and A. H. Auslender, Numerical investigation of shock-train response to inflow boundary-layer variations, *AIAA J.* **55**, 2888 (2017).
- [28] C. P. Wang, L. S. Xue, and X. Tian, Experimental characteristics of oblique shock train upstream propagation, *Chin. J. Aeronaut.* **30**, 663 (2017).
- [29] S. M. Mousavi and E. Roohi, Three dimensional investigation of the shock train structure in a convergent–divergent nozzle, *Acta Astronaut.* **105**, 117 (2014).
- [30] R. Kamali, S. M. Mousavi, and A. R. Binesh, Three dimensional CFD investigation of shock train structure in a supersonic nozzle, *Acta Astronaut.* **116**, 56 (2015).
- [31] J. S. Geerts and K. H. Yu, Three-dimensional nature of shock trains in rectangular scramjet isolators, in *Proceedings of the 54th AIAA Aerospace Sciences Meeting* (American Institute of Aeronautics and Astronautics, San Diego, California, 2016), p. 1164.
- [32] J. S. Geerts and K. H. Yu, Shock train/boundary-layer interaction in rectangular isolators, *AIAA J.* **54**, 3450 (2016).
- [33] R. L. Hunt and M. Gamba, On the origin and propagation of perturbations that cause shock train inherent unsteadiness, *J. Fluid Mech.* **861**, 815 (2019).
- [34] F. Gnani, H. Zare-Behtash, C. White, and K. Kontis, Numerical investigation on three-dimensional shock train structures in rectangular isolators, *Eur. J. Mech. B-Fluids* **72**, 586 (2018).
- [35] F. Gnani, H. Zare-Behtash, C. White, and K. Kontis, Effect of back-pressure forcing on shock train structures in rectangular channels, *Acta Astronaut.* **145**, 471 (2018).
- [36] L. M. Edelman, M. Gamba, R. Hunt, and A. Auslender, Three-dimensional structure and modeling of a normal bifurcated shock train from experimental measurements, in *Proceedings of the AIAA Scitech 2022 Forum* (American Institute of Aeronautics and Astronautics, San Diego, California, 2022), p. 0370.

- [37] H. J. Tan, S. Sun, and H. X. Huang, Behavior of shock trains in a hypersonic inlet/isolator model with complex background waves, *Exp. Fluids* **53**, 1647 (2012).
- [38] K. J. Xu, J. T. Chang, W. X. Zhou, and D. R. Yu, Mechanism and prediction for occurrence of shock-train sharp forward movement, *AIAA J.* **54**, 1403 (2016).
- [39] N. Li, J. T. Chang, K. J. Xu, D. R. Yu, W. Bao, and Y. P. Song, Oscillation of the shock train in an isolator with incident shocks, *Phys. Fluids* **30**, 116102 (2018).
- [40] N. Li, J. T. Chang, K. J. Xu, D. R. Yu, W. Bao, and Y. P. Song, Prediction dynamic model of shock train with complex background waves, *Phys. Fluids* **29**, 116103 (2017).
- [41] H. X. Huang, H. J. Tan, S. Sun, and Z. Y. Wang, Behavior of shock train in curved isolators with complex background waves, *AIAA J.* **56**, 329 (2018).
- [42] W. X. Hou, J. T. Chang, Z. Q. Xie, Y. Y. Wang, L. K. Wu, and W. Bao, Behavior and flow mechanism of shock train self-excited oscillation influenced by background waves, *Acta Astronaut.* **166**, 29 (2020).
- [43] W. X. Hou, J. T. Chang, Y. Y. Wang, C. Kong, and W. Bao, Experimental study on the forced oscillation of shock train in an isolator with background waves, *Aerosp. Sci. Technol.* **106**, 106129 (2020).
- [44] Z. A. Wang, J. T. Chang, G. W. Wu, and D. R. Yu, Experimental investigation of shock train behavior in a supersonic isolator, *Phys. Fluids* **33**, 046103 (2021).
- [45] Z. A. Wang, J. T. Chang, Y. M. Li, R. Y. Chen, W. X. Hou, J. F. Guo, and L. J. Yue, Oscillation of the shock train under synchronous variation of incoming Mach number and backpressure, *Phys. Fluids* **34**, 046104 (2022).
- [46] Z. A. Wang, J. T. Chang, W. X. Hou, and D. R. Yu, Low-frequency unsteadiness of shock-wave/boundary-layer interaction in an isolator with background waves, *Phys. Fluids* **32**, 056105 (2020).